

#### Politecnico di Torino

## Department of Environmental, Land and Infrastructure Engineering

# Master of Science in Georesources and Geoenergy Engineering

# Seismic surface wave interferometry for near surface characterization

**Candidate:** 

Daulet Magzumov

**Supervisor:** 

Prof. Farbod Khosro Anjom

#### **Abstract**

This thesis examines the use of seismic surface-wave interferometry for near-surface characterization from ambient noise records. An artificial sand body at the CNR experimental site was being monitored using a dense receiver array. By analysing the cross-correlations of ambient noise between receiver pairs, we can extract empirical Green's functions and Rayleigh-wave dispersion curves. We accessed over 7000 receiver paths and selected 2130 reliable dispersion curves for inversion. Resulting estimates were a shear-wave velocity (Vs) model within the first 5 m depth. Two types of inversion schemes were tested; unconstrained and constrained. Although a similar data misfit (≈11.7%) was achieved by both models, the Vs model resulting from the constrained inversion was found to be more realistic, as it provided a more realistic and consistent model, ranging from 100−130 m/s at the surface to 250−270 m/s at depth. Due to strong traffic noise coming from the northern direction, the noise field was irregular, which negatively impacted the reconstruction quality and limited the clear imaging of the sand body. Ambient-noise interferometry combined with constrained inversion is an effective non-invasive tool for shallow site characterization, the results confirm.

#### Acknowledgement

I would like to mention that I deeply thank my supervisor, Prof. Farbod Khosro Anjom, whose contribution to the successful completion of this thesis was through his advice and encouragement and support. In particular, I appreciate how he offered me his help, even well after his regular working hours, which speaks regarding the level of dedication he has for his students. The suggestions that he offers are very important for me. Also, his negative feedback and positive suggestions have become crucial to directing my study and getting through so many hurdles. I would like to acknowledge all the professors who helped me gain knowledge during these 2 years and I thank them for their efforts to teach and to the lectures which developed an academic outlook on me. I would like to express my deepest gratitude to my family who supported me unconditionally, who patiently understood me during my whole study period. Thanks to their limitless faith in my ability, as well as their moral support and encouragement, I did not back down from anything to complete this job. Lastly, I would also like to thank my classmates for their help in the assignment as well as the examinations. I appreciate how much assistance I have received at every stage of this project.

### **Table of Contents**

1.	Intro	Introduction				
2.	Seis	smic surface waves & Interferometric approach	9			
2	2.1	Fundamentals of Seismic Surface Waves	9			
	2.1.	1 Seismic Waves	9			
	2.1.	2 Propagation in Layered and Heterogeneous Near-Surface Media	10			
	2.1.	Near-field effects	12			
	2.1.	4 Phase & Group Velocity	13			
2	2.2	Surface-Wave Interferometry	14			
	2.2.	1 Two-Station Configuration and Cross-Correlation	15			
	2.2.	2 Dispersion Analysis and Inversion of Rayleigh Waves	20			
3.	Data	a	22			
3	3.1	Study Area and Geological Setting.	22			
3	3.2	Ambient-Noise Data Acquisition	25			
4.	Met	hodology	27			
2	1.1	Dispersion curve picking	30			
4	1.2	Inversion	33			
5.	Res	ults	35			
6.	Con	aclusions	42			
Ref	ferenc	es	43			

## **List of Figures**

Figure 2-1 Radiation pattern on body waves and seismic waves
Figure 2-2 Schematic representation of Rayleigh and Love surface waves and their
particle motion
Figure 2-3 Schematic representation of cross-correlation between two receivers
(reproduced from Wapenaar et al., 2010). (a) Source and receiver geometry; (b-c)
individual recordings at stations A and B; (d) time-domain cross-correlation 16
Figure 2-4 Example of the cross-correlation process between two ambient-noise
recordings (reproduced from Wapenaar et al., 2010). (a-b) Seismic noise records from
two different receivers showing similar wave patterns; (c) resulting cross-correlation
function (CCF)
Figure 2-5 Experimental dispersion curve (reproduced from Foti et al., 2014)
Figure 2-6 Experimental Vs model (reproduced from Foti et al., 2014)
Figure 2-7 A schematic view of how the lateral constraints are imposed in tomographic
inversion. 22
Figure 3-1 Location of the CNR test site in Turin, Italy
Figure 3-2 Geometry of the artificial sand body and receiver array layout. (a) Three-
dimensional schematic of the sand body embedded within the host medium. (b) Plan
view of the receiver configuration (120 geophones) arranged in cross-shaped and
irregular outer geometry, with the sand body. (c) Vertical cross-section showing the
trapezoidal shape of the sand body
Figure 3-3 Azimuthal and spatial coverage of the receiver array. (a) Azimuth rose
diagram showing the distribution of inter-receiver paths (b) Spatial map of all receiver
paths (green lines) connecting 120 sensors (blue dots)
Figure 3-4 Field setup of the receiver array at the CNR test site
Figure 4-1 The detailed workflow of the surface-wave interferometry process 27
Figure 4-2 Illustration of the interferometric signal-processing sequence at 25 Hz. (a)
Input seismic traces recorded at two receiver locations (T1 and T2). (b) Filtering and
cross-correlation stages showing enhancement of coherent Rayleigh-wave arrivals after
Gaussian filtering. (c) Cross-multiplication matrices in the frequency-time and
frequency-velocity domains, where the blue line correspond to the picked fundamental
mode

Figure 4-3 Dispersion energy images and picked phase-velocity curves. (a) Examples of
dispersion energy maps E(f, c) for two receiver pairs after stacking. (b) The black curve
indicate automatically phase-velocity values used for the subsequent inversion 31
Figure 4-4 The manually cleaned dispersion curve
Figure 4-5 Example of a dispersion energy image showing a non-physical upward trend.
Figure 5-1 Collection of all extracted dispersion curves
Figure 5-2 Azimuthal and spatial coverage of the selected receiver pairs. (a) Azimuth
rose diagram showing the distribution of 2130 selected receiver pairs. (b) Spatial map of
the selected paths (green lines) connecting receivers (blue dots)
Figure 5-3 The data coverage of the estimated surface wave fundamental modes of the
CNR data set as pseudo-slices corresponding to different wavelength intervals between:
(a) 0-1 m. (b) 1-2 m. (c) 2-5 m. (d) 5-10 m. (e) 10-15 m
Figure 5-4 Comparison of observed and synthetic dispersion curves for constrained and
unconstrained inversions. (a) Constrained inversion: the red lines represent the fitted
synthetic phase-velocity curves that follow the observed dispersion data (black). (b)
Unconstrained inversion: similar overall fit quality is achieved
Figure 5-5 RMS misfit evolution during inversion. (a) Constrained inversion: the global
RMS error rapidly decreases within the first few iterations and stabilizes after about the
6th iteration. (b) Unconstrained inversion: a similar convergence trend is observed, but
the model requires around 8th iteration. 39
Figure 5-6 Shear-wave velocity maps for the unconstrained inversion model. (a-e) Vs
distributions for depth intervals $0-1$ m, $1-2$ m, $2-3$ m, $3-4$ m, and $4-5$ m
Figure 5-7 Shear-wave velocity maps for the constrained inversion model. (a-e) Vs
distributions for depth intervals $0-1$ m, $1-2$ m, $2-3$ m, $3-4$ m, and $4-5$ m
List of Tables
Table 3-1 Acquisition and processing parameters used for ambient-noise interferometry
Table 4-1 Reference model used for the tomographic inversion

#### 1. Introduction

Our understanding of the subsurface is crucially important for geoscience and engineering problems. The shallow subsurface influences the ground response to both natural processes and human activity. The distribution of Vs with depth has significant correlation to mechanical characteristics of the ground. Thus, shear wave velocity is related to geotechnical parameters that describe the soil stiffness and deformation characteristics. As a consequence, Vs is one of the parameters used to classify the site, assess the seismic hazard and design the foundation and infrastructures (Foti et al., 2018).

Historically, procedures like multichannel analysis of surface waves, spectral analysis of surface waves, and borehole tests have been used to get Vs profiles for sub-surface study (Park et al., 1999, Nazarian & Stokoe, 1984, Hardin & Drnevich, 1972). These approaches often yield trustworthy outcomes, but they also require controlled seismic sources, field crews, and open areas. As a result, there is increasing interest in the passive seismic methods which rely on naturally existing vibrations as opposed to artificial sources.

The term "ambient noise" refers to any kind of continuous vibration of the ground. This may occur due to natural or human activity. This includes wind, sea waves, rainfall, traffic, or due to some machinery. Over the last 20 years, scientists have proven that this background noise can provide useful seismic information with the help of seismic interferometry (Campillo & Paul, 2003, Snieder, 2004). By taking long recordings between the two sensors and cross-correlating them, the Green's function of the medium can be reconstructed with one of the sensors acting as a source (Campillo & Paul 2003; Wapenaar 2004; Shapiro & Campillo 2004). This helps us extracting coherent surface waves mainly Rayleigh waves and studying their velocity variation as a function of frequency. The information can be subsequently employed to evaluate exceeding the Groupspeed at Vs with depth (Bensen et al., 2007; Wapenaar et al., 2010).

At the near-surface scale, surface-wave interferometry allows us to image shallow layers with good resolution and without using any active sources (Luo et al., 2015). Yet, in small-scale field experiments, the ambient noise is rarely used to depict Vs model. More often than not, energy comes from nearby and directional sources (e.g. roads and buildings), which serve to distort the symmetry of the cross-correlations (Halliday & Curtis, 2008). Another challenge is that the inversion of dispersion curves is a non-unique

problem, meaning that distinct velocity models may similarly predict the same data (Tarantola, 2005). To stabilize results, neighboring models are often enforced to have spatial structure or performance criteria consistent with physics.

The aim of this work is to apply surface-wave interferometry for investigating the near-surface structure of an artificial sand body at the CNR experimental site located in Turin (Italy). A controlled environment is offered by this site, where geometry and material properties are known, allowing the performance of the method to be assessed in isolation. We deployed a dense grid of three-component (30) and one-component (90) geophones to continuously record noise.

In Chapter 2, the theoretical framework is presented. The chapter gives the important properties of surface waves, Rayleigh-wave dispersion and interferometric principle to obtain Green's functions from the ambient-noise cross-correlation.

Description of the field experiment and dataset in Chapter 3. The geological and geometrical of CNR experimental site in Turin is discussed together with the layout of the receiver array and the characteristics of the recorded ambient noise.

The details of processing workflow and inversion method are given in Chapter 4. The chapter discusses the extraction of dispersion curves and their inversion for shear-wave velocity profiles. Two inversion strategies are compared: unconstrained and constrained inversion, where each 1D model is computed independently.

Finally, Chapter 6 provides the concluding remarks. The study shows that surface-wave interferometry can be a cost-effective, non-invasive way of imaging shallow subsurface materials. Future research possibilities include better designs for the arrays, monitoring the noise source, and using newer inversion strategies.

#### 2. Seismic surface waves & Interferometric approach

This chapter defines the movement of surface waves propagating near the surface and what can be studied from their behavior. It describes basic propagation behavior and outlines the variations at depth. Furthermore, it describes the seismic interferometric that allows to use ambient background noise to investigate the subsurface.

#### 2.1 Fundamentals of Seismic Surface Waves

#### 2.1.1 Seismic Waves

When the energy is propagated through or along the surface of a medium, which comes from various sources that can be used at the surface, the periodic vibrational disturbance will occur, which will be called seismic waves. Such waves are classified into two basic groups: body waves which widely propagate, forming an isotropic radiation pattern from a source, and the surface waves which move along a free surface. Surface waves movement is parallel to the earth surface, and their attenuation with depth obey an exponential form.

Surface waves have many properties that make them particularly suitable for geometrical characterization. They have a much lower rate of geometric attenuation than body or bulk waves, and this is because the energy of body waves spreads spherically , while surface waves propagates cylindrically (Figure 2.1-1).

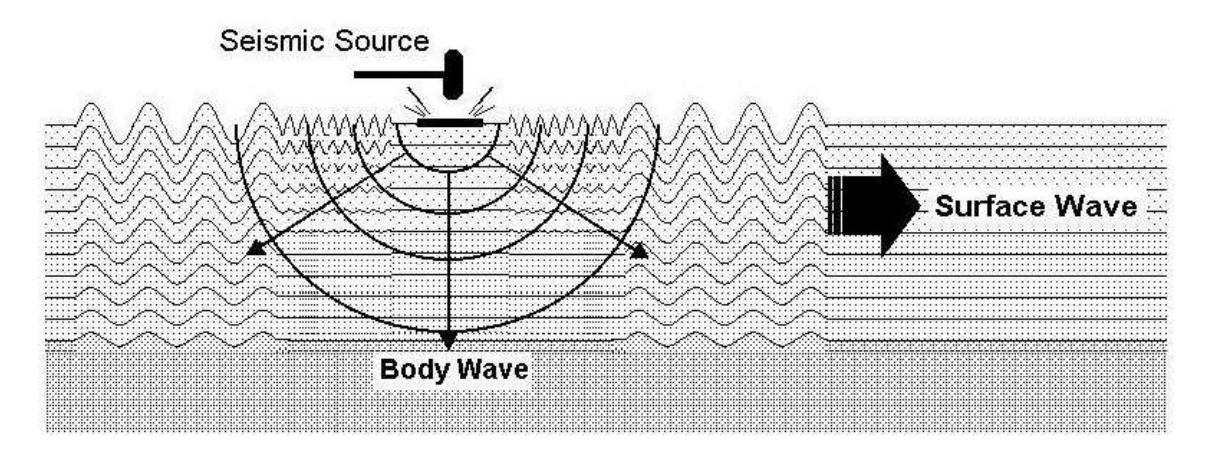


Figure 2-1 Radiation pattern on body waves and seismic waves.

There are two main types of surface waves — Rayleigh and Love waves. Vertically polarized surface waves were theoretically described by the British physicist Lord John Strutt Rayleigh in 1885, and the Love wave was later deduced by the mathematician A. E. H. Love, who generated the horizontal transverse oscillation orthogonal to the propagation direction (Rayleigh, 1885; Love, 1911). Rayleigh waves travel along the earth's ground with a more complicated kinematic pattern than Love waves. The motion of individual particles follows an elliptical retrograde path, meaning that they move opposite to the direction of wave propagation. Because it rolls, it moves the ground up and down, and forward and backward in the direction that the wave is moving as shown in Figure 2.1-2.

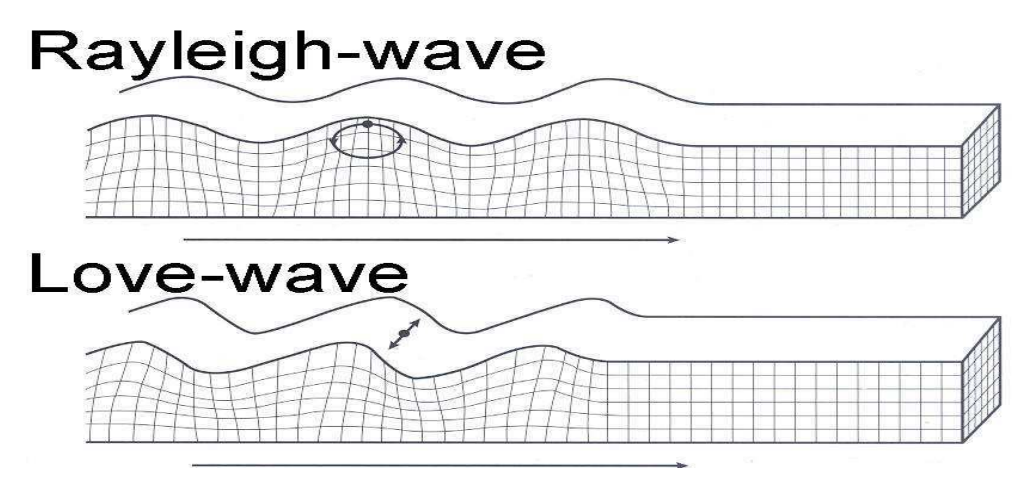


Figure 2-2 Schematic representation of Rayleigh and Love surface waves and their particle motion.

Because of their relatively high simplicity for its generation and detection at the ground, Rayleighs waves have customarily been employed for surface-wave testing. Similarly, utilizing the so-called Love waves which are derived from horizontally polarized surface movements is also possible but with limitations regarding layer stratigraphy and the difficulties involved to produce Love waves (Foti et al., 2014).

#### 2.1.2 Propagation in Layered and Heterogeneous Near-Surface Media

Since the upper layers of the soil are loose, it has high porosity and low density, and with increasing depth, the rock becomes denser due to compaction and cementation, resulting in an increase in density and bulk modulus.

Shear wave velocity can be calculated as (Lipinski et al., 2017):

$$V_S = \sqrt{\frac{\mu}{\rho}},\tag{2.1}$$

where,  $\mu$  is the shear modulus and  $\rho$  is the density. Despite that, shear velocity is inversely proportional to the density, it is controlled primarily by shear stiffness which tends to grow rapidly comparing to density as depth increases.

A medium through which a Rayleigh wave travel can be either homogeneous or heterogeneous. In a homogeneous half-space, where material properties stay constant with depth, they move at one constant velocity that does not depend on frequency. In contrast, for the heterogeneous medium the wavefield is much more complex. The wave frequencies of the short wavelengths are mostly restricted to the softer soils near the top, while the frequencies of the long wavelengths penetrate deeper into the stiffer soils, propagating at the corresponding higher wave velocity. This phenomenon is known as *geometric dispersion*.

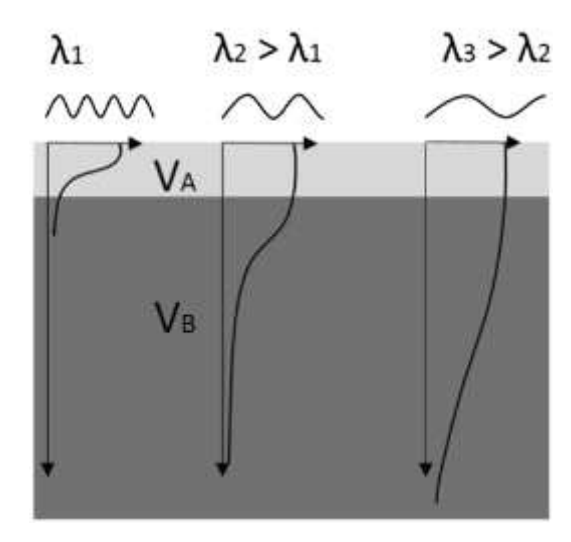


Figure 2.1-3 Geometric dispersion of surface waves in vertically heterogeneous media (reproduced from Foti et al., 2018).

Figure 2.1-3 shows a horizontally layered medium having 2 separate layers, with different physical properties. Three Rayleigh waves is given with a high, mid, and low-frequency, corresponding to large, medium and short wavelengths. Starting with a wave with a highest frequency on the left, the particle motion is basically confined in the soft top layer. In the middle, the longer wavelength penetrates deeper and samples the soft layer of upper part as well as partly stiffer part of the lower layer of the surface. In the end, wave with the lowest frequency wave extends way out into the stiffer lower layer and propagates in the higher velocity material.

Additional lateral heterogeneities such as abrupt facies changes, buried channels, or manmade structures may further disturb the wavefield by scattering or refracting the wavefronts. For a number of engineering-geophysical applications, it is common to have a single-dimensional layered model. However, in strongly heterogeneous environments such a model will represent only a partial representation of the real wave behaviour. A complete understanding of these propagation phenomena is essential in the correct interpretation of dispersion curves and in the reliable inversion of dispersion curves in order to obtain the shear wave velocity profiles.

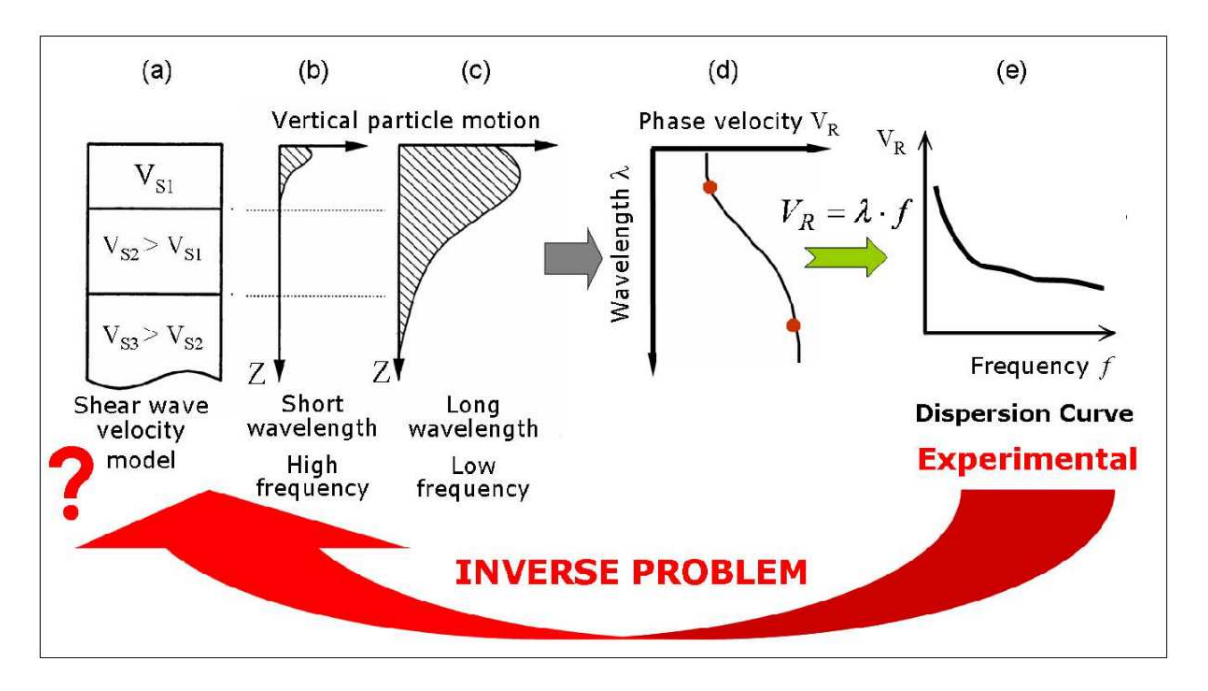


Figure 2.1-4 Illustration of the surface-wave dispersion and inversion process. (a) Shear-wave velocity model composed of layers with increasing Vs; (b) Short wavelengths (high frequencies) are sensitive to shallow layers; (c) Long wavelengths (low frequencies) penetrate deeper; (d) Relationship between phase velocity  $V_R$  and wavelength  $\lambda$ ; (e) Experimental dispersion curve showing the decrease of phase velocity with frequency.

The concept of frequency-dependent penetration depth, velocity increase with wavelength, and inversion problem is schematically illustrated in Figure 2.1-4.

#### 2.1.3 Near-field effects

Although Rayleigh waves can give important information on the vertical variation of stiffness, it should be noted that at very short offsets or high frequencies, near-field effects may also interfere into the wavefield being recorded, and the true dispersion behaviour will be distorted. These appear when a source and receiver are too close with respect to the wavelength of the propagating Rayleigh wave.

The wavelength is defined as:

$$\lambda = \frac{V_R}{f} \tag{2.3}$$

where  $V_R$  is the Rayleigh-wave velocity and f is the frequency.

At values of the offset less than one wavelength ( $\Delta x < \lambda$ ), the motion recorded contains not only the propagating surface-wave component but also non-propagating near-field terms, these terms being related to the quasi-static deformation about the source. (Aki & Richards, 2002; Foti et al., 2018).

These elements strongly decays as distance and results in phase distortions which ends up with overestimation of the phase velocity and in most cases creates an artificial increase to the high-frequency portion of the dispersion curve. To minimise this effect, the distance between the source and the first receiver should be at least one to two wavelengths of the analysed frequency range (Park et al., 1999).

#### 2.1.4 Phase & Group Velocity

That frequency-dependent behaviour of Rayleigh waves follows the dispersive nature of the propagation of surface waves in layered media (Foti et al., 2017). Whereas geometric dispersion relates to the properties of various frequencies exploring different depths, complete description of dispersive behaviour needs a distinction between phase velocity and group velocity.

The phase velocity  $(V_p)$  demonstrates the rate of each frequency unit or a point of constant phase of the wave. It is mathematically defined as:

$$V_p = \frac{\omega}{k},\tag{2.4}$$

where  $\omega$  is the angular frequency and k is the wavenumber (Aki and Richards, 2002).

Through the study of phase shifts at a sequence of frequencies, it is possible to obtain the experimental dispersion curve by determining  $V_p(f)$ . This curve links observable wave behaviour to the subsurface structure: each point on the curve corresponds to an average stiffness over the depth range sampled by that frequency. The group velocity  $(V_g)$  is defined as:

$$V_g = \frac{d\omega}{dk} \tag{2.5}$$

represents the velocity at which the overall wave energy or the envelope of the signal propagates (Aki and Richards, 2002).

Despite most of field dispersion analyses not directly plotting group velocity, it determines the energy distribution and travel time of a dispersion of recorded surfacewave train.

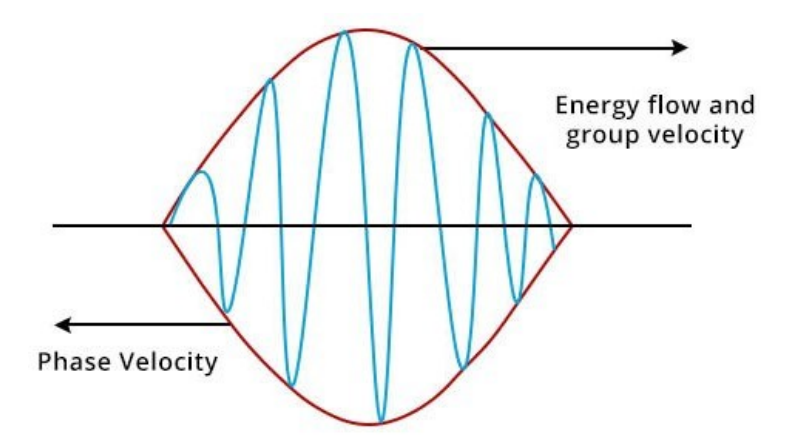


Figure 2.1-5 Phase and group velocity representation in a wave packet.

Assuming the two superposing waves have similar frequencies, waveform will have a high frequency wave inside a low frequency envelope. The crests of the high frequency part travel at the velocity of  $\frac{\omega}{k}$  but the envelope at the velocity of  $\frac{d\omega}{dk}$ .

Figure 2.1 4: schematically depicts the idea of phase velocity and group velocity. The distinction between the two kinds of velocities is very pronounced in very dispersive media, where the wave packet is dispersed over time. The knowledge of this difference can explain why the highest amplitude of the signal can have a slight discrepancy with the observable movement of the phase on a seismogram.

#### 2.2 Surface-Wave Interferometry

In practice, the controlled seismic sources may be unavailable. The surface of the earth is always in motion as a result of natural activities and human activities that include waves of the oceans, wind, traffic, and prior to industrial activities. Such continuous vibrations that are also termed as *ambient seismic noise* can be used as a natural source of information on the subsurface. Every location in the environment may be viewed as a weak and random source emitting the waves in all directions. In case of a large number of such sources operating concurrently and being mutually uncorrelated, their overall effect is a diffuse wavefield which spreads to the receivers in many directions.

This property makes it feasible to obtain the response between two receivers which called the Greens function, by cross-correlating the recordings of noise on them. This principle is represented out in successive sections, beginning with a perfect impulsive case and other more realistic band-limited and noise-based cases successively.

#### 2.2.1 Two-Station Configuration and Cross-Correlation

Seismic interferometry (SI) is a signal processing technique that is used to synthesize the wave field between the two receivers as one of them were in practice a virtual source. Basically, it involves cross-correlating records taken at two receiver positions with each other, which illustrates the function of the Green the impulse response that would indicate how waves would propagate between one receiver to another through the same medium (Wapenaar et al., 2010).

This principle relies on the fact that the two receivers are in a common section of the same wave path as in the source of the wave. By the cross-correlation of their documented wavefields, the common path cancels, and a remainder term is produced which is proportional to the travel time separating receivers themselves. As a result, a single receiver is able to recreate the direct wave, without knowing the actual origin of the signal source or when it was emitted, which will increase the usefulness of interferometry to application in ambient-noise measurements and passive imaging (Wapenaar et al., 2010).

Interferometric principle is demonstrated in the following by working an ideal impulsive case step by step and then generalizing the results to the case of band-limited and noise based. The examples show that the functionality of the Green between two receivers can be recovered based on the recorded signals.

#### 2.2.1.1 Impulsive case

Direct-wave interferometry may be illustrated by a one-dimensional geometrical model of an impulsive source (Fig. 2.3). In this case, a point source at location,  $x_S$  results in a delta pulse that travels through a homogeneous medium, which has a single fixed velocity c. The two receivers will be aligned on the same axis at coordinates  $x_A$  and  $x_B$  ( $x_A < x_B$ ). The wavefront emitted arrives at receiver A, as at time,  $t_A = |x_A - x_S|/c$ , and receiver B as at time,  $t_B = |x_B - x_S|/c$ . The signals recorded at the receivers are thus delta-shaped Green's functions  $G(x_A, x_S, t) = \delta(t - t_A)$  and  $G(x_B, x_S, t) = \delta(t - t_B)$  (Wapenaar et al., 2010).

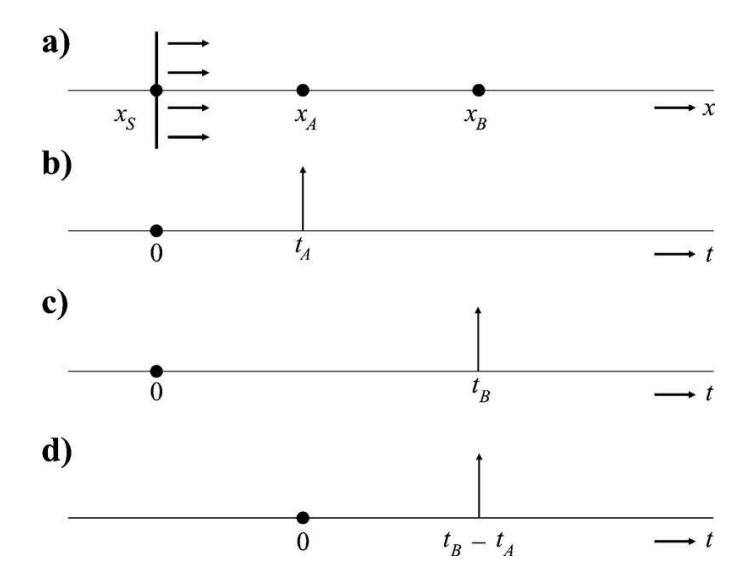


Figure 2-3 Schematic representation of cross-correlation between two receivers (reproduced from Wapenaar et al., 2010). (a) Source and receiver geometry; (b–c) individual recordings at stations A and B; (d) time-domain cross-correlation.

Figure 2.2-1 schematically shows this geometry. The spatial arrangement of the upper panel in Figure 2.2-1(a) is a depiction of the source S and receivers A and B; panels in Figure 2.2-1(b) and in Figure 2.2-1(c) is a depiction of the associated impulses recorded at each receiver separated in time by a time delay which is proportional to the difference in distance between the two receivers; panel in Figure 2.2-1(d) is a depiction of what would result by correlating the two traces indicating a working correlation maximum at a time lag proportional to the difference in distance between the two receivers.

The cross-correlation is mathematically described as,

$$C_{AB}(t) = [G(x_B, x_S, \cdot) \star G(x_A, x_S, -\cdot)](t) = \int G(x_B, x_S, \tau) G(x_A, x_S, \tau - t) d\tau \quad (2.6)$$

and the latter reversed in time, so that the times of arrival coincide. The correlation functional reaches its peak at time delay of the form of time shift at  $t_B - t_A$ . The resulting peak appears at a positive time lag

$$t = t_B - t_A = \frac{|x_B - x_A|}{c}$$
 (2.7)

corresponding to the propagation of a direct wave from A to B. Such positive time correlation peak is the causal feature of the inter-receiver Green function,  $G_{AB}(t)$ .

Assuming the source was at the other side, receiver B would record the wave sooner than receiver A,  $t = t_A - t_B < 0$ , which would peak at the correlation between the two via the

anti-causal component of the signal,  $G_{AB}(-t)$  (Snieder, 2007). Therefore, time lags are positive when energy flows at A to B and are negative when energy flows at B to A.

This process is successful in removing the typical propagation path between the source and the two receivers as well as isolating the segment between them:

$$G(x_{R}, x_{A}, t) = G(x_{R}, x_{S}, t) \star G(x_{A}, x_{S}, -t)$$
 (2.8)

The signal obtained is the same as the record that would otherwise be seen in the event that a virtual source were positioned at point A and the noise signal at point B (Wapenaar et al., 2010). This one-dimensional illustration shows clearly that the correlations between two records give both the causal and the anti-causal constituents of the Green function between receivers and thus forms the theoretical basis of seismic interferometry.

#### 2.2.1.2 Non-impulsive (band-limited) case

In practical applications, the emitted signal is rarely a perfect delta impulse; instead, it has a finite duration and limited spectral content, represented by the source wavelet s(t). The wavefields which are recorded by receivers A and B are, therefore, the product of the Green functions with the source signal:

$$u(x_A, t) = G(x_A, x_S, t) \star s(t) \tag{2.9}$$

$$u(x_B, t) = G(x_B, x_S, t) \star s(t) \tag{2.10}$$

On cross-correlation of these two recorded signals, the ensuing expression will be

$$u(x_{B},\cdot) \star u(x_{A},-\cdot) = G_{AB}(t) \star S_{S}(t) \tag{2.11}$$

and  $S_s(t) = s(t) \star s(-t)$  represents the auto-correlation of the source wavelet.

The use of the term proves that retrieved inter-receiver Green,  $G_{AB}(t)$  is convolved with the source autocorrelation meaning that the amplification prior to reconstruction is band limited under the frequency content of the emitted wavelet (Wapenaar et al., 2010; Snieder, 2007).

In practice therefore, this constraint limits the bandwidth of the interferometric output which can be utilized as well as determining the time resolution which can be achieved on the reconstructed Green function.

#### 2.2.1.3 Ambient noise case

When a medium is under sustained excitation by stochastic energy source, then wavefield recordings are mainly filled with ambient seismic noise. The contribution of each individual source is of weak vibrations, but the summation of all sources in due course results in the useful information about the features of the propagation of the medium. By recording this continuous noise at two receivers at the same time, the cross-correlation of the two recordings serves to isolate the coherent arrivals in common to both traces and hence provide a good representation of the impulse response, or the function of Green, at the two receiver positions.

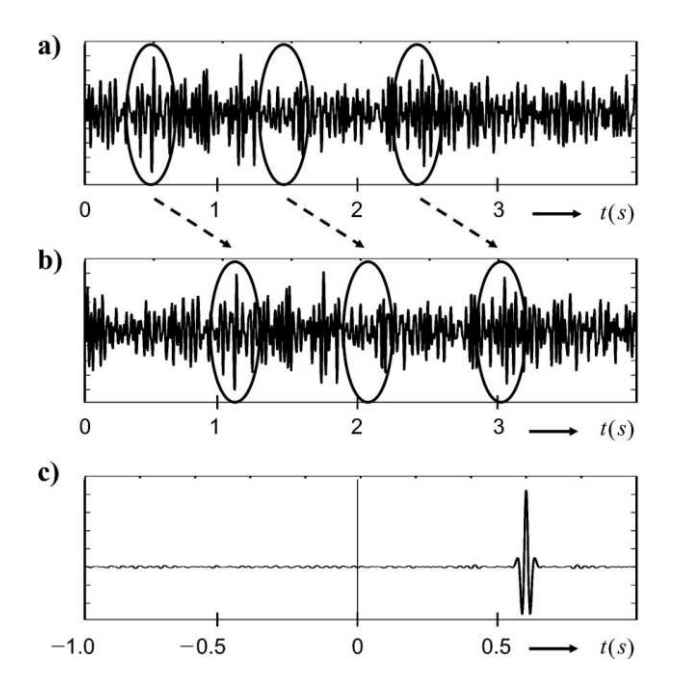


Figure 2-4 Example of the cross-correlation process between two ambient-noise recordings (reproduced from Wapenaar et al., 2010). (a–b) Seismic noise records from two different receivers showing similar wave patterns; (c) resulting cross-correlation function (CCF).

Figure 2.2-2 illustrates this process. Panels (a) and (b) show two noise recordings at receiver A and B respectively, which had similar wavelets at different times, which were caused by random sources. The associated outcome of cross-correlation is shown in panel (c) in which the coherent arrivals are visible at negative and positive time lags. The positive lag peak is that resulting where propagation occurs between A and B, and that of the negative lag is the propagation in the reverse direction.

Mathematically, the noise recording correlation could be termed as

$$C_{AB}(t) = \langle u(x_B,t) \star u(x_A,-t) \rangle_T \approx [G_{AB}(t) + G_{AB}(-t)] \star S_N(t)$$

in which,  $u(x_B, t)$  and  $u(x_A, t)$  are the signals of the noise and  $S_N(t)$  is the autocorrelation of the ambient field (Wapenaar et al., 2010).

This expression is the basis of passive seismic interferometry, which allows the reconstruction of the Green's function between two receivers without an active source being used. The procedure works best when the noise sources are not correlated, the recording times are long enough to accomplish statistical averaging and the illumination is essentially isotropic in all directions (Bensen et al., 2007).

The main goal in direct-wave interferometry is to measure the delay time between two receivers which is proportional to the surface wave travel time between the receivers. Once this travelling time has been determined, the mean velocity of propagation could be deduced based on the known distance between the receivers. Practically, the technique is used not just in single time measurements, but also in a range of frequencies, thus allowing to determine the phase velocity as a function of frequency.

In two and three dimensional geometries, the retrieved Greens function remains the direct wave between receivers, but it is built up by the addition of efforts of many directions of sources on the surface. In higher dimensions, the direct-wave component can only be recovered correctly when the illumination and path coverage is sufficient enough to cover all the relevant propagation directions in the result of the correlation (Wapenaar et al., 2010).

Various critical conditions have to be met before the interferometric correlation can reproduce the function of the Green.

- (1) Sufficient averaging time. Long recording times are needed in order that incoherent signals be canceled whilst coherent arrivals to the true propagation of waves between receivers take the prevalence.
- (2) Balanced illumination. In a one-dimensional set-up the waves are to be received on both sides of the receiver pair so that both the causal and anticausal are recovered and so the result of the correlation is symmetrical.
- (3) Uncorrelated noise sources. The ambient noise should have independent action hence the disappearance of cross-terms in a correlation following time averaging and retaining only the physically significant component of the wavefield.

Under this set of conditions, cross-correlation provides a consistent and true estimate of the receiver-receiver Green. Breaks of such assumptions on the other hand, e.g. biased illumination, insufficient recording time, and noise sources that are highly correlated may cause distortions or partial wavefield recovery (Wapenaar et al., 2010; Campillo and Roux, 2015).

#### 2.2.2 Dispersion Analysis and Inversion of Rayleigh Waves

A combination of filtered signals is used to create a dispersion image, in which frequency (or period) is plotted as horizontal axis, phase velocity as vertical axis, and amplitude (or energy) is encoded by the colour intensity. Figure 2.2-3 is used to show the distribution of surface-wave energy with the frequencies and velocities. The frequencies of the greatest energy are determined in each frequency, and a sequence of frequency-velocity pairs is found that characterize the experimental dispersion curve c(f). This curve is a representation of the apparent phase velocity versus the frequency which is a way of showing the differences between the elasticity of the layers and the stiffness in the ground.

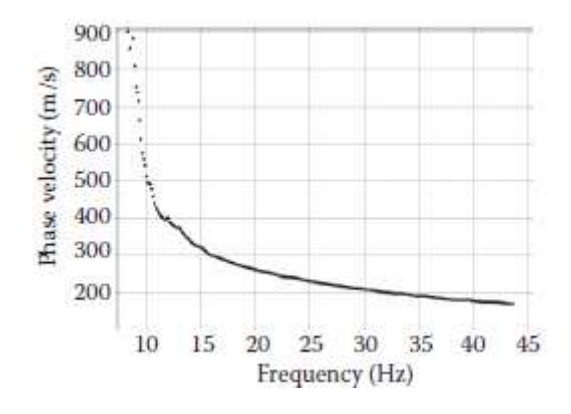


Figure 2-5 Experimental dispersion curve (reproduced from Foti et al., 2014).

When a dispersion curve that has been obtained through the experiment is finally extracted, it can be inverted to make an approximation of the shear-wave velocity profile,  $V_S(z)$ . The observed dispersion behaviour and the material properties are inversely related, meaning we can try to find the velocity structure that best explains the data that we measure.

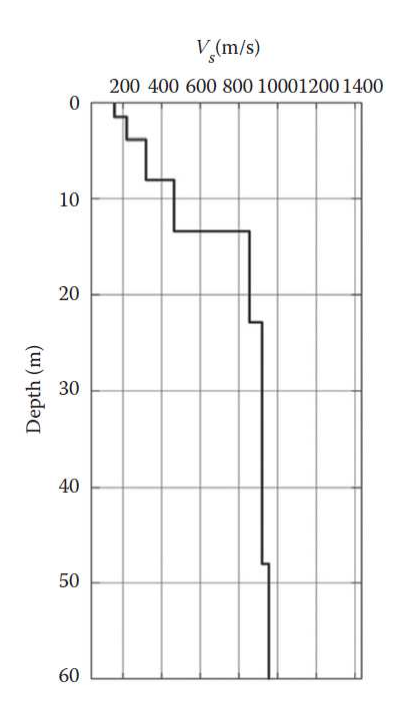


Figure 2-6 Experimental Vs model (reproduced from Foti et al., 2014).

In the simplest case, a one-dimensional (1D) inversion is performed for every receiver pair to obtain a vertical velocity profile (Figure 2.2-4). Since each frequency is sensitive to a certain depth range, this process successfully translates the frequency-dependent phase velocities into a depth-consolidated shear-wave velocity model. The 1D profile that results from inversion demonstrates how stiffness becomes higher with depth. We generally observe lower values of  $V_s$  in near-surface unconsolidated materials followed by greater velocities in deeper, dense materials.

When dispersal information is accessible for numerous receiver matching. Individual 1D solutions can be spatially blended through tomographic inversion to reconstruct vertical and lateral stiffness variations. This process creates a continuous two dimensional or three dimensional display of the near-surface with contrasting mechanical properties.

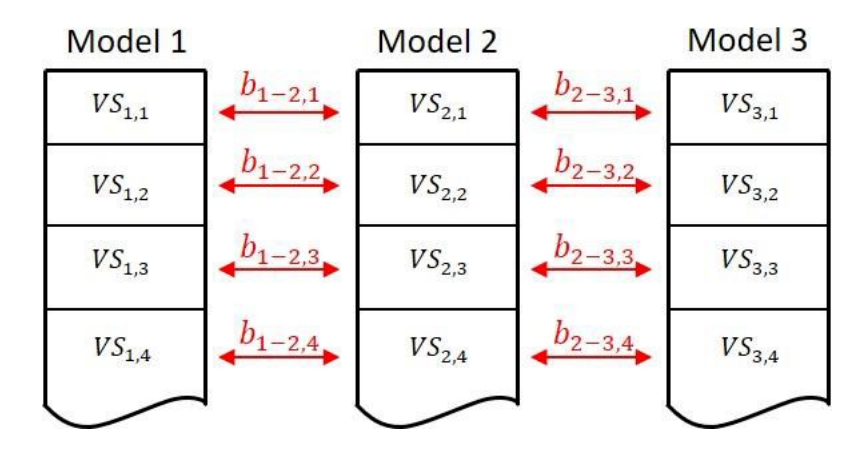


Figure 2-7 A schematic view of how the lateral constraints are imposed in tomographic inversion.

Different models can fit just as well to the observed data due to the non-unique nature of the inversion process. To achieve physically meaningful results, regularization and constraints are applied, typically smoothness or damping terms which will stabilize the solution and prevent unrealistic jumps in the velocity field.

These constraints link the shear-wave speed of each model point to its adjacent models' velocities, limiting abrupt lateral discontinuities while retaining true structural contrasts as illustrated in Figure 2.2-5. This coupling is such that final velocity field will vary smoothly across the tomographic grid.

The tomographic inversion is a physical process which results in a stiffness map (of the sub-surface) via the frequency-dependent propagation of Rayleigh waves. Deeper and stiffer layers are sampled by lower frequencies and shallower frequencies by higher frequencies. The V<sub>s</sub> producing distribution accounts for vertical gradient and lateral (horizontal) heterogeneities needed for site characterization and geotechnical work. In other words, tge V<sub>s</sub> distribution being featured is realistic as well as continuous. (Foti et al. 2018; Socco et al., 2010).

#### 3. Data

#### 3.1 Study Area and Geological Setting

The experimental field work was in CNR test site of Turin, Italy (Figure 3.1-1). The site has an artificial body of sand embedded in the Po Plain alluvial deposits as shown in Figure 3.1-1 (red square). The sediments are alternating layers of gravel, fine sediments and sand.

At the surface, the sand body occupies an area of approximately  $5 \times 5$  m, but gets down to a depth of approximately 2.5 m with a tapered trapezoidal form (Figure 3.1-2(a)).

The top layer of sands is loose and highly porous with low values of P and S-wave velocities and lower stiffness compared to the surrounding materials which are denser and more consolidated. This strong lateral velocity contrast makes the location especially well adapted to such testing techniques that are sensitive to the heterogeneities in the near surface.



Figure 3-1 Location of the CNR test site in Turin, Italy.

In order to measure the ambient-noise wavefield over the sand body, a hybrid receiver array was put in place. The structure consisted of a cross shaped central part with other receivers introduced around it at a random arrangement. Figure 3.1-2 (b) shows that total of 30 three-component and 90 one-component geophones were placed in a region with outer dimensions of  $21.6 \times 20.84$  m whilst the real receiver coverage amounted to approximately 331 square meters.

To make a complete cross shape over the artificial sand body, the receivers were planted to make two perpendicular lines at regular interval. The distance between the receiver was 0.75 m in the horizontal direction and 0.5 m in the vertical direction. The other receivers were located in a irregular pattern in quasi-random order around the center. This pattern resulted in an overall increase of the average receiver spacing in the array to approximately 9 m distance thus creating a larger aperture while still allowing sufficient coverage of surface-wave interferometry.

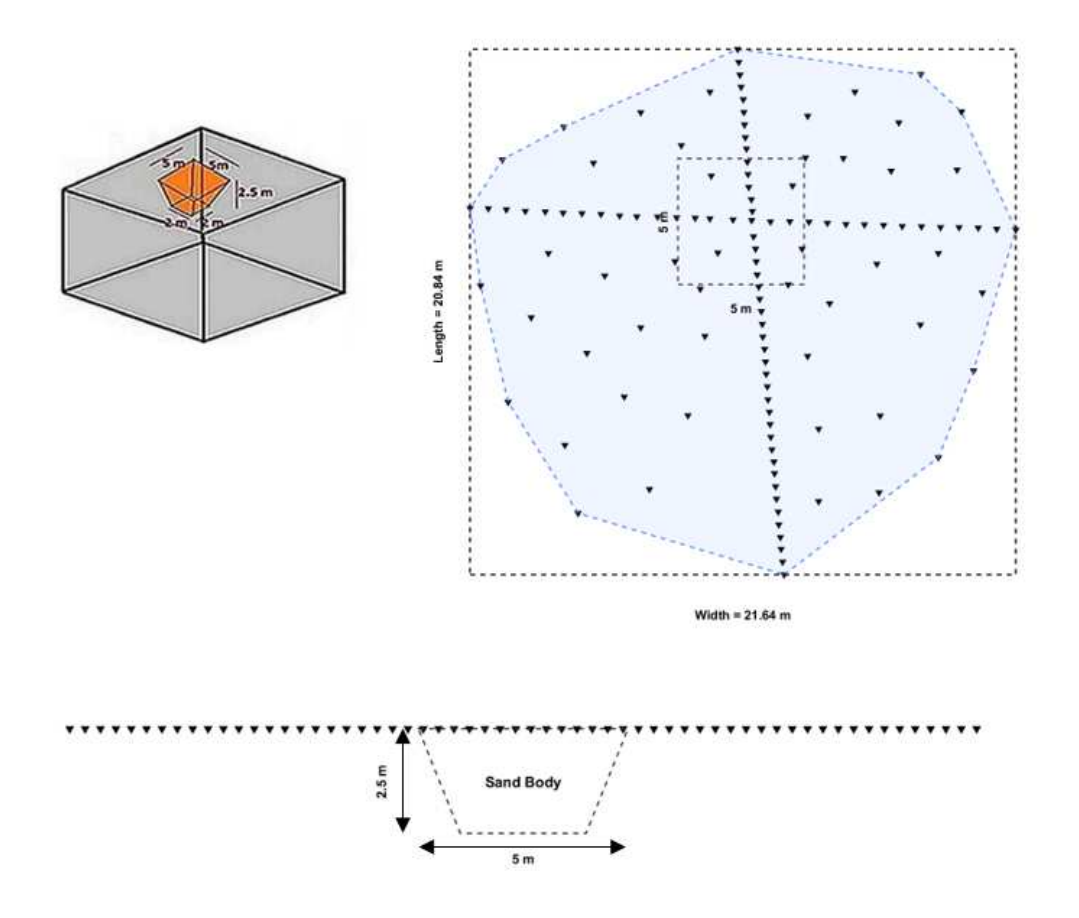


Figure 3-2 Geometry of the artificial sand body and receiver array layout. (a) Three-dimensional schematic of the sand body embedded within the host medium. (b) Plan view of the receiver configuration (120 geophones) arranged in cross-shaped and irregular outer geometry, with the sand body. (c) Vertical cross-section showing the trapezoidal shape of the sand body.

Azimuthal rose diagram was created through which the distribution of all the pairs of the receivers in the array was indicated. Overall, 7,140 interstation paths were available by taking into account all combinations of receivers. The diagram is covered by an azimuth of 0° to 180°, whereas the reference intervals are 250, 500, 750 and 1000 paths. There are two different directional patterns almost at 90° and 180°, with the east-west and north-south directions of a central cross. The total number of paths is approximately 700 around 90° and progressively over 1,000 around 180°, which shows the greatest alignment in these major axes. For most other azimuths, the number of paths stays close to 300, indicating a relatively even coverage provided by the irregular outer array.

The geometrical arrangement makes the array achieve the ambient-noise wavefields over many directions and therefore minimizes directional bias and increases the stability and reliability of the interferometric outcomes.

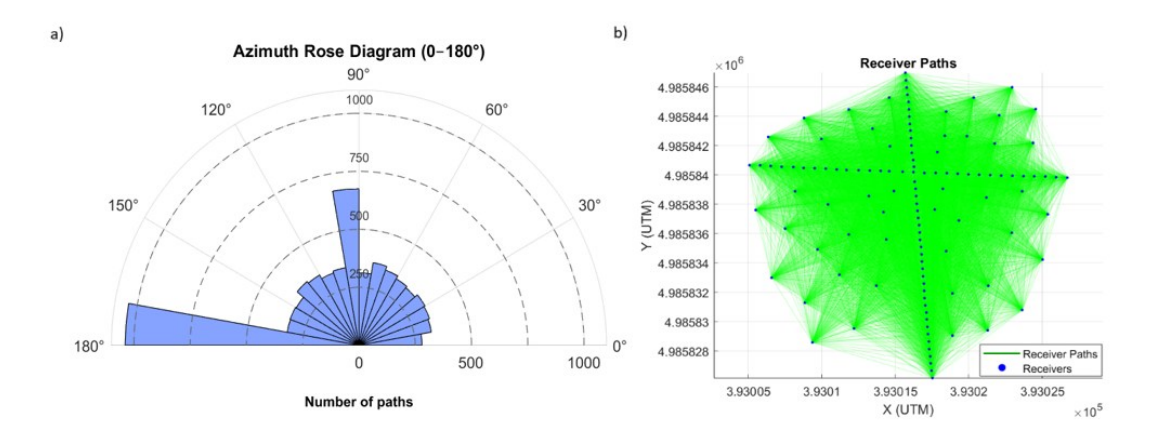


Figure 3-3 Azimuthal and spatial coverage of the receiver array. (a) Azimuth rose diagram showing the distribution of inter-receiver paths (b) Spatial map of all receiver paths (green lines) connecting 120 sensors (blue dots).

#### 3.2 Ambient-Noise Data Acquisition

Figure 3.2-1 shows that constant ambient-noise measurements were carried out at the CNR Site with a high intensity of 120 receivers. The system was in continuous mode, hence, providing a stable acquisition that favors further ambient-noise interferometry. The signals that were recorded involved both the low-frequency microtremors and the intermediate-frequency anthropogenic vibrations, which provided the broadband input suitable in the retrieval of the functions of Rayleigh-wave Green. Table 3 -1 gives a brief description of the acquisition and processing parameters.

Table 3-1 Acquisition and processing parameters used for ambient-noise interferometry

Parameter	Value		
Number of time samples	2501		
Sampling interval	0.001		
Gaussian smoothing factor	0.15		
Frequency range	2:5:100		
Velocity range	50:1:700		
Stacking limit	5		
Maximum inter-station offset	400		



Figure 3-4 Field setup of the receiver array at the CNR test site.

#### 4. Methodology

The workflow proposed for surface-wave interferometry is aimed at deriving near-surface shear-wave velocity (V<sub>s</sub>) model from ambient-noise recordings through a continuous sequence of processing steps (Figure 4-1). The process includes preparing the data, processing the interferometric signals, extracting the dispersion curves and performing tomographic inversion. Every step taken was performed such that coherence of reconstructed Rayleigh waves was maintained and the inversion results were reliable.

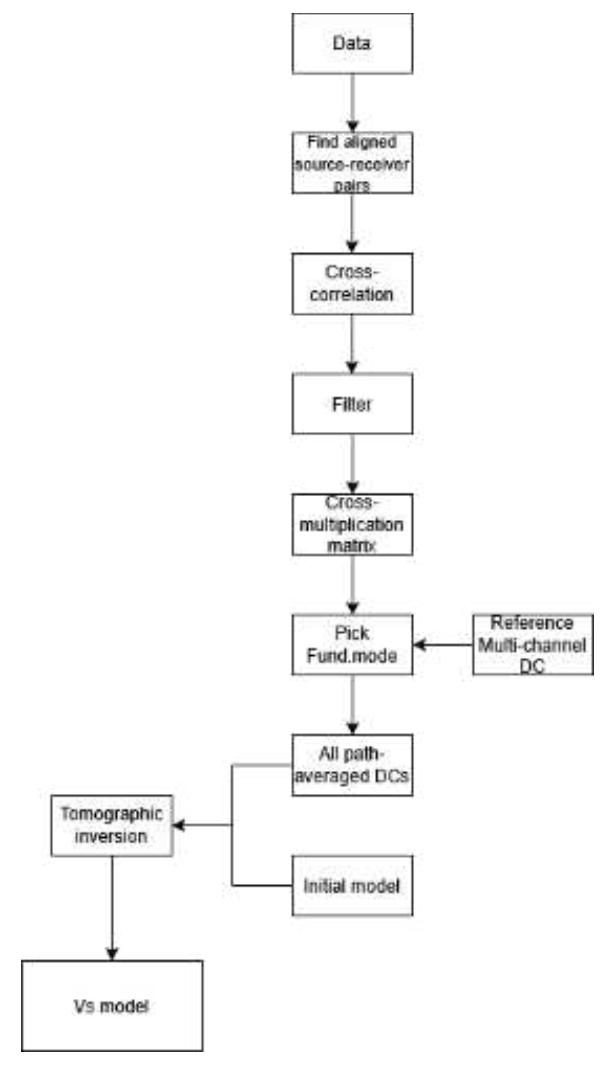


Figure 4-1 The detailed workflow of the surface-wave interferometry process.

The receiver array consisting of 120 geophones studied can theoretically form 7 140 paths of any two stations. However, in practice only 3570 unique paths were processed. It was decided to keep redundancy low and computationally not heavy while ensuring representivity in the dataset. The dense arrangement of receivers led to many pairs having very similar azimuths and small offsets. It turns out that keeping only half of the

combinations will achieve full spatial and azimuthal coverage without repetitions of reciprocal or geometrically equivalent conditions.

Noise records were cross-correlated for each valid pairs to obtain the empirical Green's function between them. The diffuse ambient field is changed into virtual shot gathers with coherent Rayleigh-wave arrivals. A multiple-Gaussian band-pass filter in the frequency domain was applied to clean the signals, which were selected within the range of 2-100 Hz and with a relative width of  $\sigma=0.15$ . Every 0.5 Hertz, a Gaussian window was centreed and all together summed to produce the smooth composite transfer function that has equal weight in the passband. This filtering step improves the energy of surface-waves while suppressing unwanted low- and high-frequencies.

Filtered traces were placed into a cross-relation matrix in the frequency-time domain, which was transformed into the frequency-velocity domain. The pattern of dispersion can be easily visualized using this representation, which also allows automatic extraction of the main Rayleigh mode.

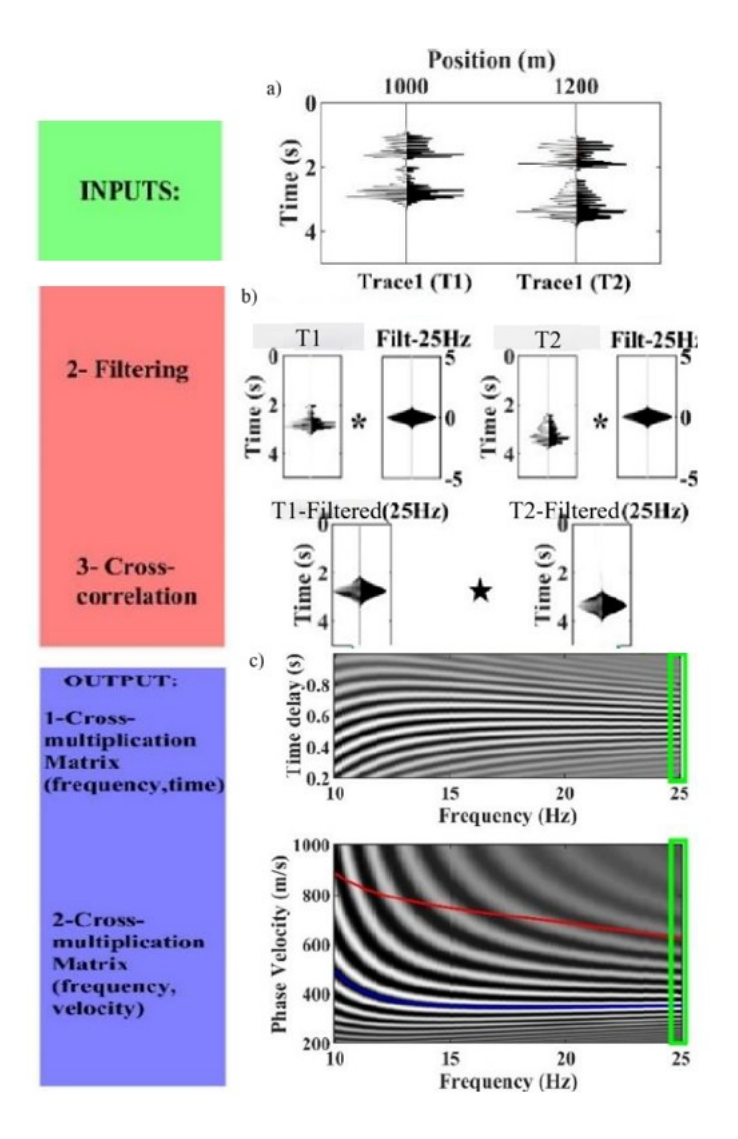


Figure 4-2 Illustration of the interferometric signal-processing sequence at 25 Hz. (a) Input seismic traces recorded at two receiver locations (T1 and T2). (b) Filtering and cross-correlation stages showing enhancement of coherent Rayleigh-wave arrivals after Gaussian filtering. (c) Cross-multiplication matrices in the frequency—time and frequency—velocity domains, where the blue line correspond to the picked fundamental mode.

The complete sequence of interferometric processing steps is illustrated in Figure 4-2, which shows the transition from the input seismic traces to the filtered and cross-correlated signals, followed by the construction of the cross-multiplication matrices in both the frequency—time and frequency—velocity domains. This operation is performed for the 25 Hz component as illustrated in the figure, which isolates the coherent Rayleighwave energy progressively and identifies the fundamental mode. Thus, the cross multiplication matrices explicitly reveal the variation of phase velocity as a function of frequency, allowing to recognize the fundamental Rayleigh mode in the examined bandwidth.

After the fundamental-mode dispersion curves were recognized along all valid paths, they were assembled to form a collection of path-averaged dispersion curves (DCs). The DCs show how fast the wave travels for each path between stations and that's the main data set for the inversion tomography.

To recover the spatial distribution of shear-wave velocity, the set of path-averaged DCs and initial model were finally introduced into the tomographic inversion algorithm. The inversion was optimized iteratively until convergence of the recorded and calculated dispersion data. The  $V_s$  model obtained provides a quantitative image of the near-surface stiffness variations and captures the main features of the investigated artificial sand body at the CNR test site.

#### 4.1 Dispersion curve picking

The main issue was to identify the dispersive behavior of Rayleigh waves in the near-surface layers. The procedure is illustrated in detail using receiver pair #3570 as a selected example because it provides a strong signal that is coherent enough to show all steps involved in the extraction of the dispersion-curve.

The dispersion energy image in Figure 4.1-1(a) depicts the amplitude of the cross-correlation as a function of frequency and phase velocity. Bright colors (yellow) are in areas where energy is big, while soft colors (blue) are low-amplitude noise areas. The map represents a clear ridge with high amplitude that falls downwards from the right to the left. The lower frequencies (8-15 Hz) are getting closer to 400-450 m/s, while the higher frequencies (60-70 Hz) are closer to about 150 m/s. This ridge represents the fundamental Rayleigh-wave mode. These green points refer to reference curves.

To objectively trace this ridge, an automatic picking function was applied. The result, shown as the black line in Figure 4.1-1(b), represents the automatically detected dispersion curve for pair 3570. The algorithm successfully follows the main trend of decreasing velocity with increasing frequency. However, at the frequency limits more 60 Hz it deviates. Because of this, additional manual refinement was required. When extracting the dispersion curve in a manual way, we have only picked the ridge corresponding to the fundamental mode (marked in red) as valid as shown in Figure 4.1-2.

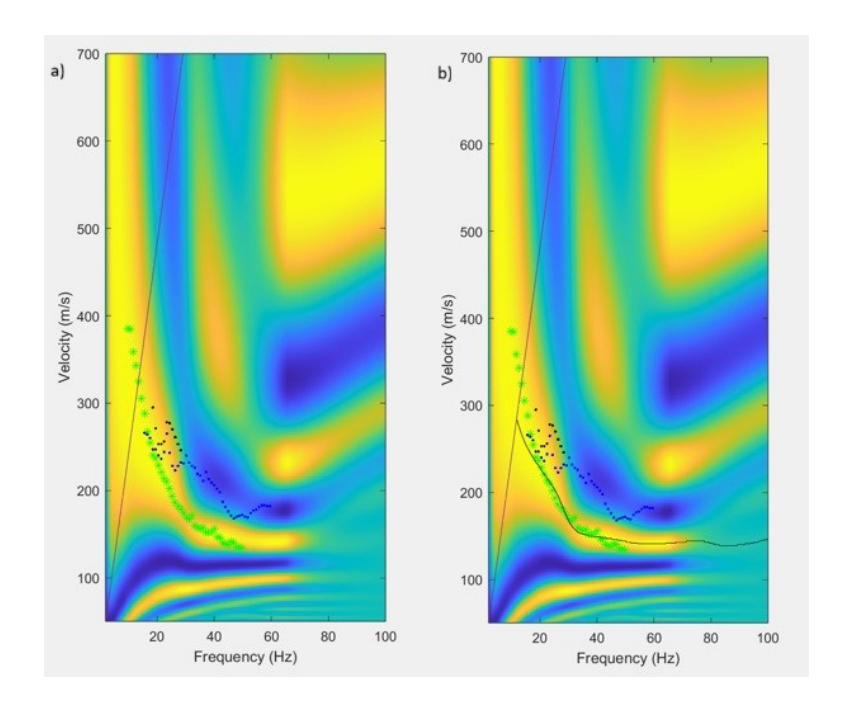


Figure 4-3 Dispersion energy images and picked phase-velocity curves. (a) Examples of dispersion energy maps E(f,c) for two receiver pairs after stacking. (b) The black curve indicate automatically phase-velocity values used for the subsequent inversion.

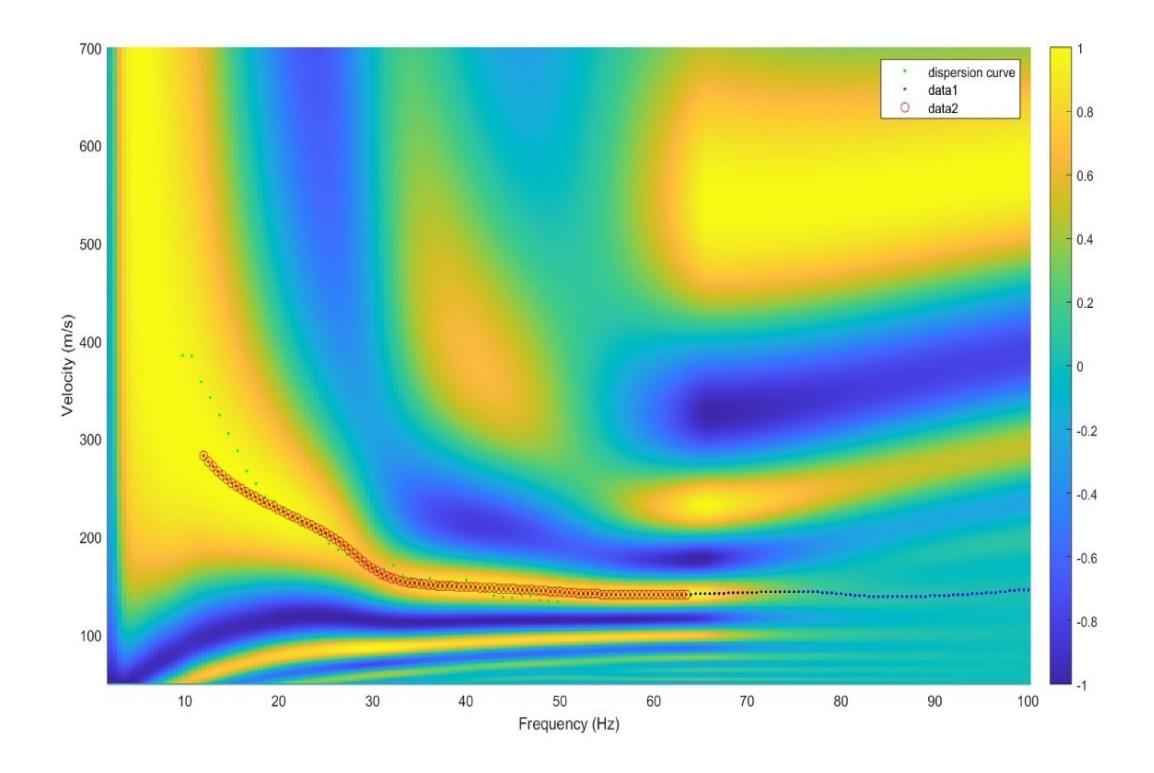


Figure 4-4 The manually cleaned dispersion curve

In certain receiver pairs, the dispersion energy image exhibited non-physical upward trends. During these trends, the apparent phase velocity increased with frequency, rather than decreasing as would be expected. As shown in Figure 4.1-3 below. The high energy

ridge is inverted and has phase velocities starting from 0 m/s at 15 Hz and reaching nearly 250 m/s at 100 Hz. The behaviour contradicts the expected Rayleigh-wave dispersion relation, which states that lower frequencies correspond to higher velocities due to deeper sampling of stiff layers.

The upward curve here is most likely due to misidentification of the fundamental mode. Sometimes, if stations are too close to each other, then there is not sufficient phase accumulation causing the group-velocity trend to become ambiguous. The automatic picking algorithm, following local amplitude maxima, incorrectly traced this inverted ridge, leading to an unrealistic dispersion curve.

Data with such anomalies were systematically excluded from the final dataset because they can severely bias the tomographic inversion and cause unrealistic velocity gradients. Only curves that showed stability, and downward monotonic dispersion was selected for analysis.

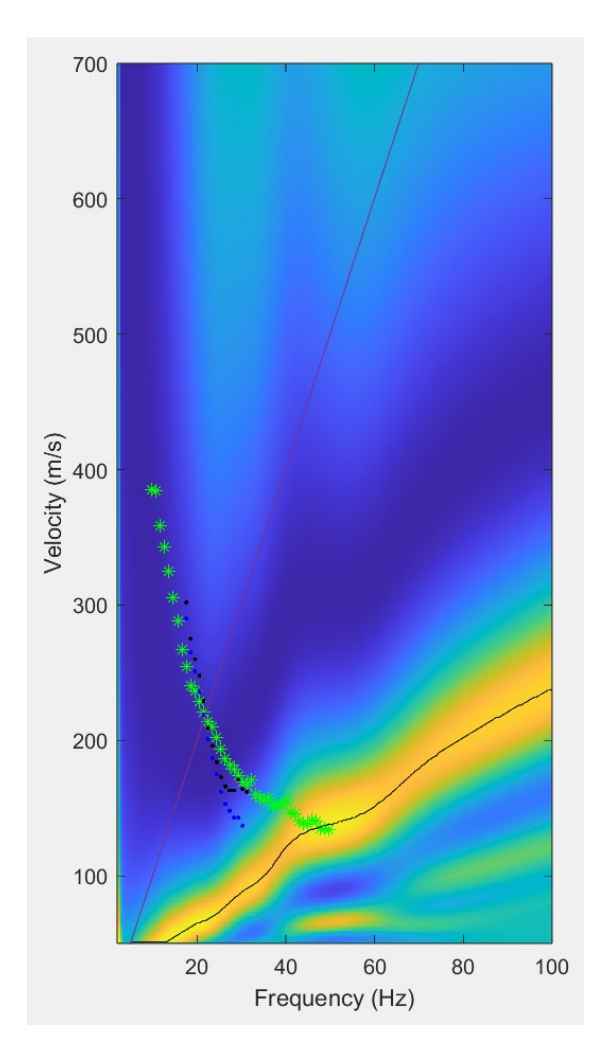


Figure 4-5 Example of a dispersion energy image showing a non-physical upward trend.

#### 4.2 Inversion

The tomographic inversion used local 1D velocity profiles from dispersion-curve inversions for creating a continuous 2D model of the near-surface shear-wave velocity  $(V_s)$ . The aim of this stage was to reproduce the lateral stiffness variations and also create a spatially consistent model of the shallow subsurface over the study area.

The adopted formulation is similar to what was proposed by Boiero (2009). Datasets that consist of path-averaged dispersion curves (DCs) like those from ambient-noise interferometry are particularly suitable for this method. In this framework, we interpret each dispersion curve as measuring the average phase velocity (or slowness) along the inter-station path connecting two receivers. All these paths, when joined, give an inversion that yields a vector distribution most compatible with the entire data set with smooth lateral changes between neighbouring cells.

The inversion began with the definition of a reference model composed of five layers of thickness of 1 m each above the surface to a total depth of 5 m. Approximately 100 independent 1D points were used for the inversion. They were evenly distributed across the area of interest in a uniform grid with 2 m spacing in both horizontal and vertical directions. Two inversion configurations were tested. In unconstrained inversion, each point was inverted independently. Constrained inversion involving smoothness constraints between neighbouring cells to enforce lateral consistency. The parameters of the model are shear-wave velocity, Poisson's ratio, and density. Out of all of these, during inversion, only  $V_s$  was allowed to vary. Poisson's ratio and density was kept constant at lab-measured and previously obtained fixed values.

The initial (reference)  $V_s$  model was defined from the mean of all 1D inversions and modified according to the general dispersion trend of the study area. The reference model parameters that are summarized in Table 4.4-1.

Table 4-1 Reference model used for the tomographic inversion.

Layer	Thickness (m)	V <sub>s</sub> (m/s)	Poisson's ratio	Density
				$(kg/m^3)$
1	1	40	0.2	1600
2	1	100	0.2	1600
3	1	140	0.33	1800
4	1	180	0.33	1800
5	1	220	0.33	1800
Half-space	-	700	0.33	1800

To help achieve a suitable model the tomographic inversion was formulated as a regularized weighted least-squares problem that minimizes the misfit between observed path-averaged dispersion data and synthetic data while imposing smoothness on the model. The objective function combines two terms.

- (a) the data misfit measures how well the predicted phase velocities match the measured dispersion curves.
- (b) the spatial regularization which penalizes large velocity gradients between adjacent model nodes.

The result is that final model fits data within its uncertainty and is therefore geologically reasonable and spatially continuous. The weighting matrix which accounts for the data misfit takes into consideration the uncertainty of the measurements and correction of each dispersion point based on wavelength.

#### 5. Results

The key results generated by the surface-wave interferometry analysis are presented in this section, including selection of dispersion curves, assessment of azimuthal and wavelength coverage and inversion to produce shear-wave velocity  $(V_s)$  structure for the area of interest. The previous section presented a workflow that was useful to reconstruct the shallow subsurface velocity field down to around 5 m depth.

The plot in Figure 5-1 shows all 2130 dispersion curves that were ultimately selected from among 3570 receiver pairs. Curves that were excluded usually appeared to be driven by strong noise that caused a lot of irregularity or an upward trend in velocity. In the dataset, a general behaviour is observed which seems to be quite consistent. The phase velocity decreases from about 400–450 m/s at the lowest frequencies considered about 15 Hz to about 100–200 m/s at frequencies above 50 Hz. The hundreds of overlapping curves that fall along the same downward trend validate the picking.

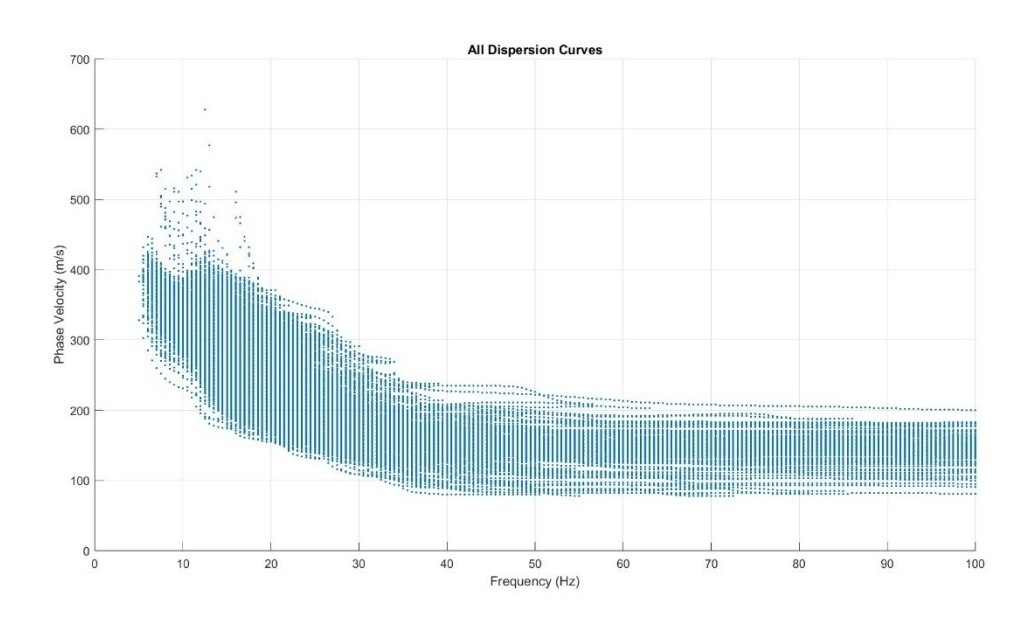


Figure 5-1 Collection of all extracted dispersion curves.

After picking the valid receiver pairs, the azimuthal and spatial coverage is checked so that the data still represents the whole array. It is observed that in the original configuration, there are about 700 paths concentrated around 90° and more than 1000 around 180°, which indicates the presence of two strong dominant directions. As represented in the final selection and depicted in Figure 5-2(a), the azimuth distribution became much more uniform. The weak peaks located near the angles of 90° and 180° are still present, although the gap between these peaks and remaining peaks have now become

much smaller So, that coverage is more evenly distributed, and results are not biased towards any one direction.

The new receiver-path map of Figure 5-2(b) also shows this. The overall cross shape of the array was maintained and the paths still span almost the entire area, but the network seems less dense because the noisy and redundant pairs were filtered out. Nonetheless, the rest of the paths are spaced out evenly and connected well so that there can be considerable spatial averaging and the dispersion analysis is representative of general site behaviour as opposed to just a few directions.

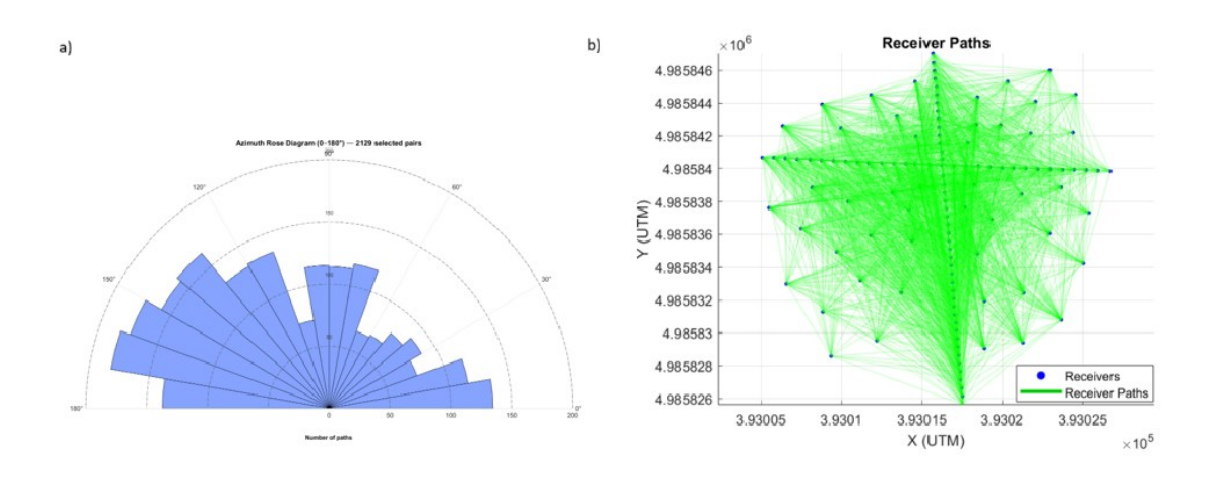


Figure 5-2 Azimuthal and spatial coverage of the selected receiver pairs. (a) Azimuth rose diagram showing the distribution of 2130 selected receiver pairs. (b) Spatial map of the selected paths (green lines) connecting receivers (blue dots).

The wavelength coverage of the estimated dispersion curves is related to the resolution and depth of investigation of tomographic inversion. For the average apparent phase velocity colour, the available inter-station paths for each wavelength range are shown. This gives a reasonable visual clue about the spatial sensitivity of the inversion.

The coverage as shown in the figure keeps increasing with wavelength. A few receiver pairs with smaller offsets is limited at the source for shorter wavelengths ( $\lambda$  < 2 m). Thus, the resolution for the shallowest layers is lower. Within the 2–10 m wavelength range (Figure 5-3(c) and 5-3(d)), the coverage becomes much denser and the data set is optimally sampled in the top 5 m. For longer wavelengths ( $\lambda$  = 10–15 m, Figure 5-3(e)), the coverage is still spatially continuous, although it becomes less thick, suggesting decreasing sensitivity to depth.

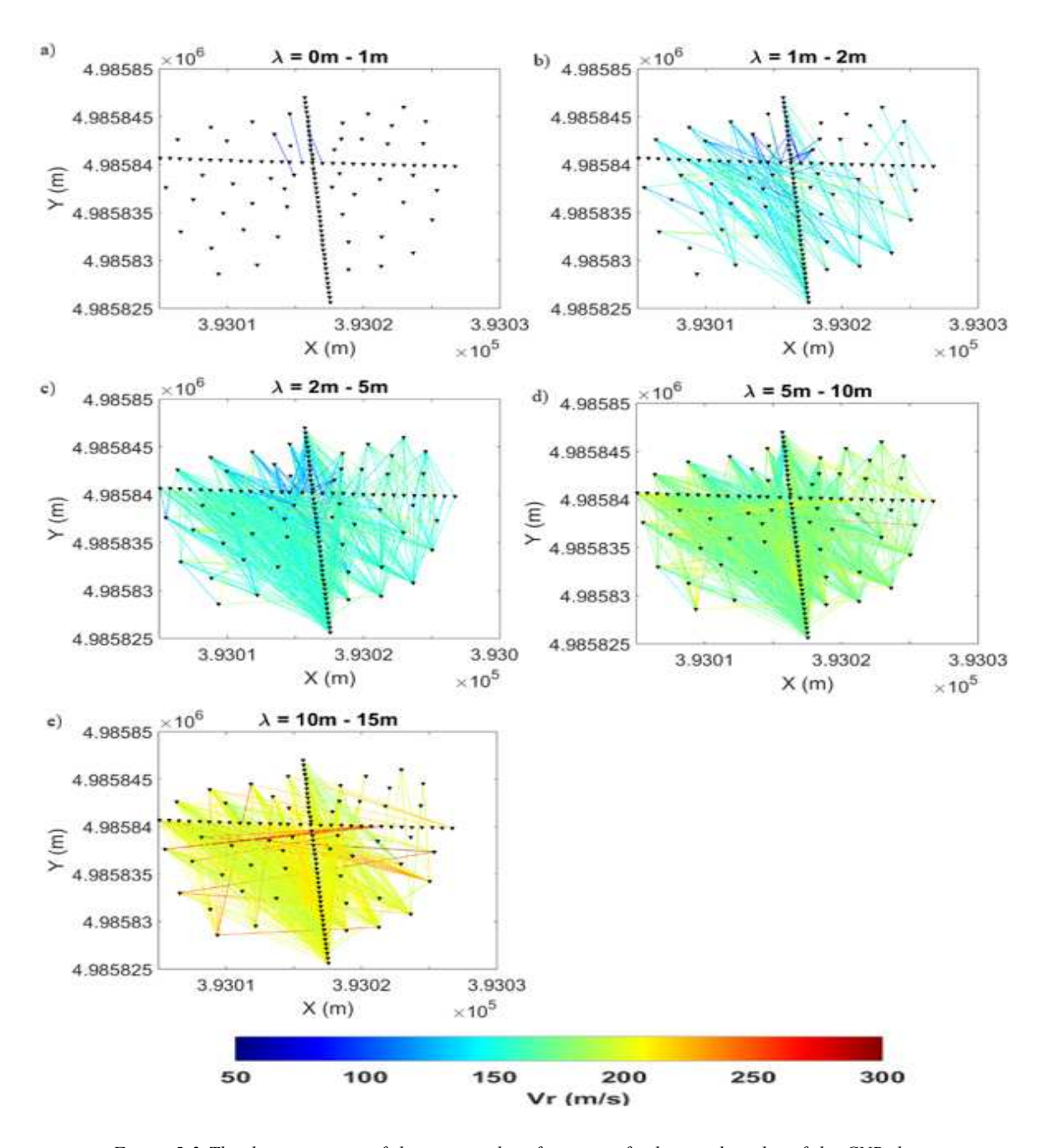


Figure 5-3 The data coverage of the estimated surface wave fundamental modes of the CNR data set as pseudo-slices corresponding to different wavelength intervals between: (a) 0-1 m. (b) 1-2 m. (c) 2-5 m. (d) 5-10 m. (e) 10-15 m

After obtaining the dispersion curves, the next step was to obtain shear-wave velocity (Vs) distribution in the study area. The Rayleigh-wave dispersion curves were inverted to change the frequency-velocity information into a shear velocity model describing the variation of stiffness with depth and laterally across the site.

As seen in the Figures 5-4(a) and 5-4(b), a comparison of the experimental (black) and synthetic (red) dispersion curves is given for the constrained and unconstrained inversions, respectively. In general, synthetic dispersion curves well matched real data,

indicating that the inversions approached similar and reliable results, with a normalized misfit of about 11.7%.

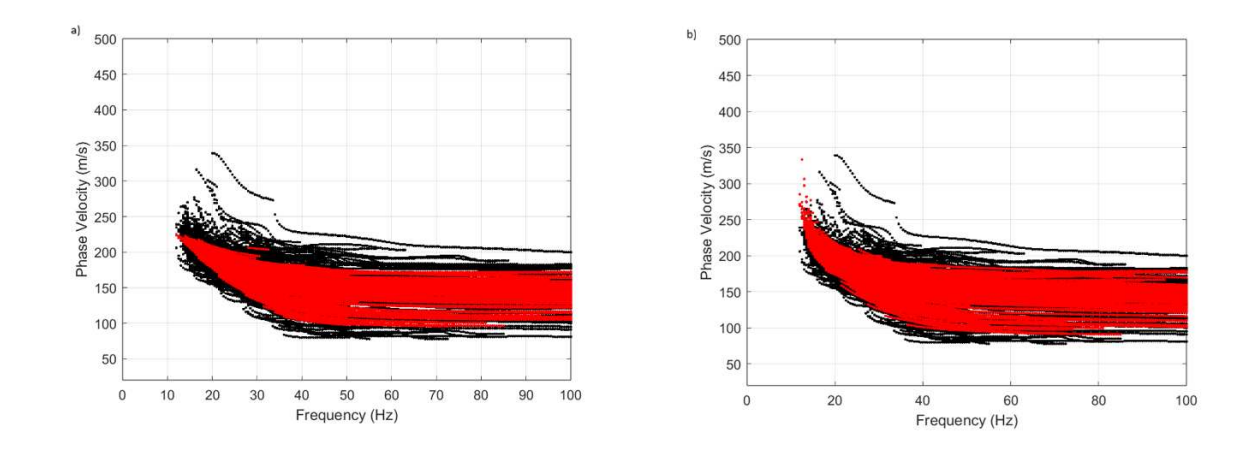


Figure 5-4 Comparison of observed and synthetic dispersion curves for constrained and unconstrained inversions. (a) Constrained inversion: the red lines represent the fitted synthetic phase-velocity curves that follow the observed dispersion data (black). (b) Unconstrained inversion: similar overall fit quality is achieved.

The convergence plots presented in Figure 5-5 show the reduction of error during iterations. For the constrained inversion (Figure 5-5(a)), the misfit became stable after the sixth iteration. However, for the unconstrained case, the misfit remained constant after the eighth one (Figure 5-5(b)). This shows both methods reached stable solutions, but the constrained inversion converged a little faster.

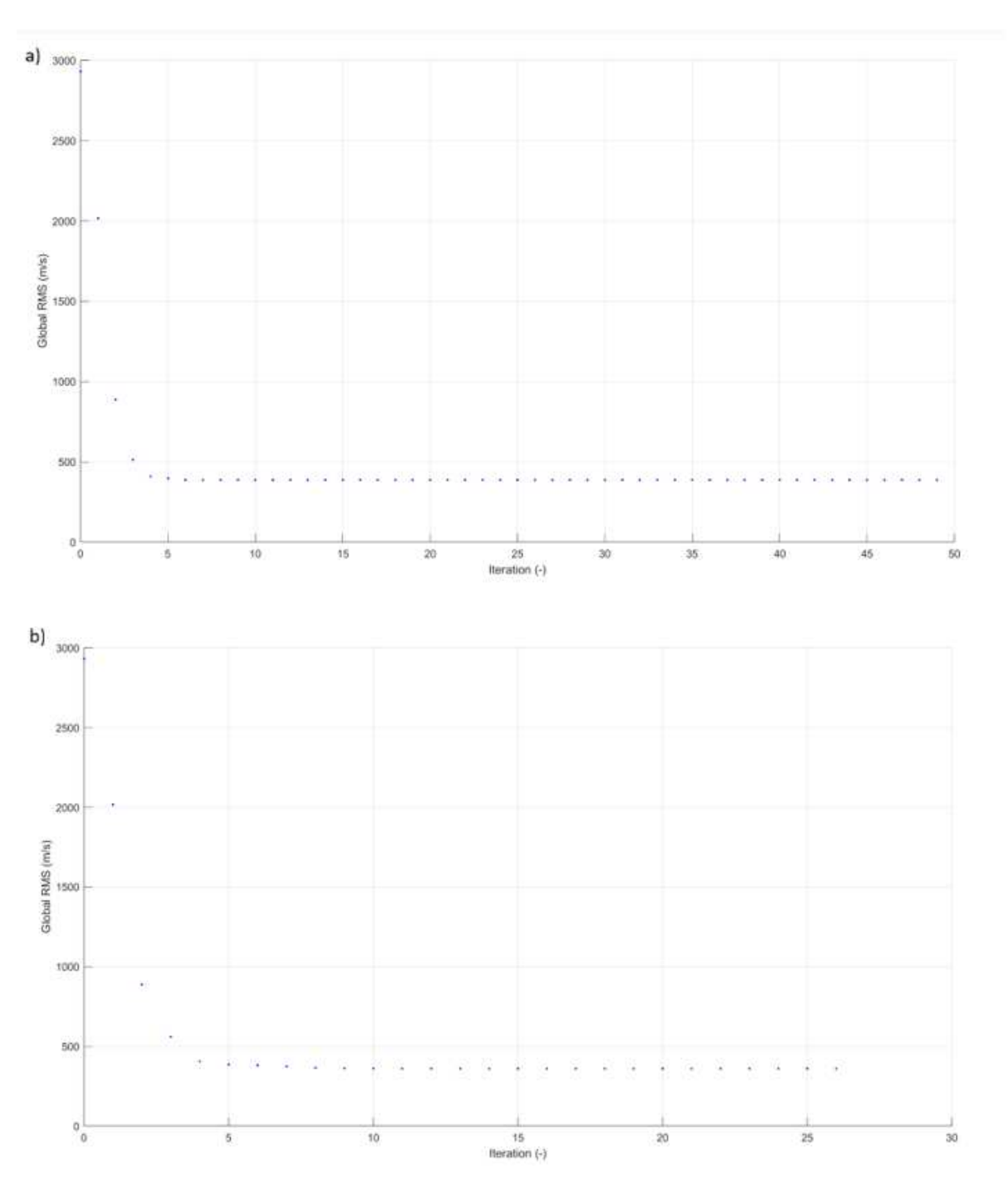


Figure 5-5 RMS misfit evolution during inversion. (a) Constrained inversion: the global RMS error rapidly decreases within the first few iterations and stabilizes after about the 6th iteration. (b) Unconstrained inversion: a similar convergence trend is observed, but the model requires around 8th iteration.

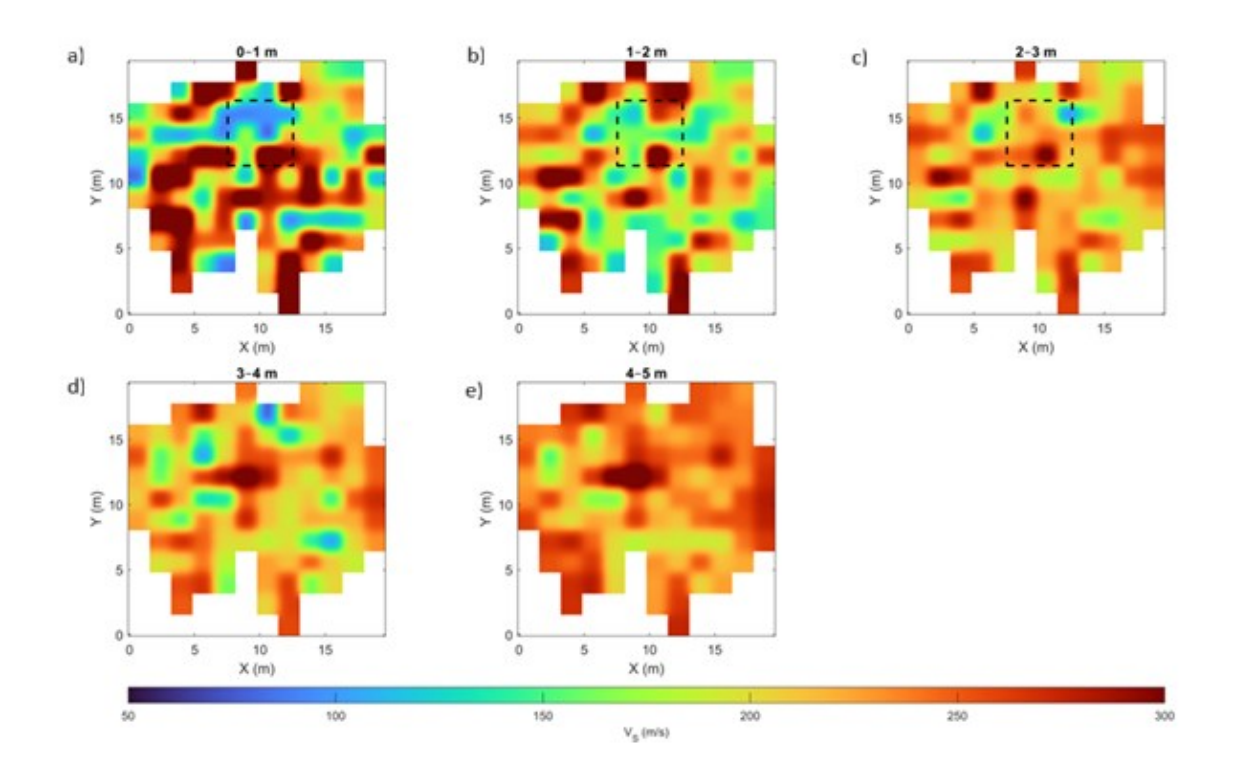


Figure 5-6 Shear-wave velocity maps for the unconstrained inversion model. (a–e) Vs distributions for depth intervals 0-1 m, 1-2 m, 2-3 m, 3-4 m, and 4-5 m.

The Vs maps in the unconstrained inversion (Figure 5-6) appear considerably noisier and less continuous. There are sharp velocity differences between neighboring cells, especially in the top 0-2 m, where Vs switches rapidly between low (~100 m/s) and high (>250 m/s) values. Without spatial smoothing, each inversion in one dimension operates independently. That means even a small amount of noise in the data leads to strong local changes in velocity. At the depths of 3 to 5 meters, the model becomes fairly stable although unrealistic fluctuations still exist.

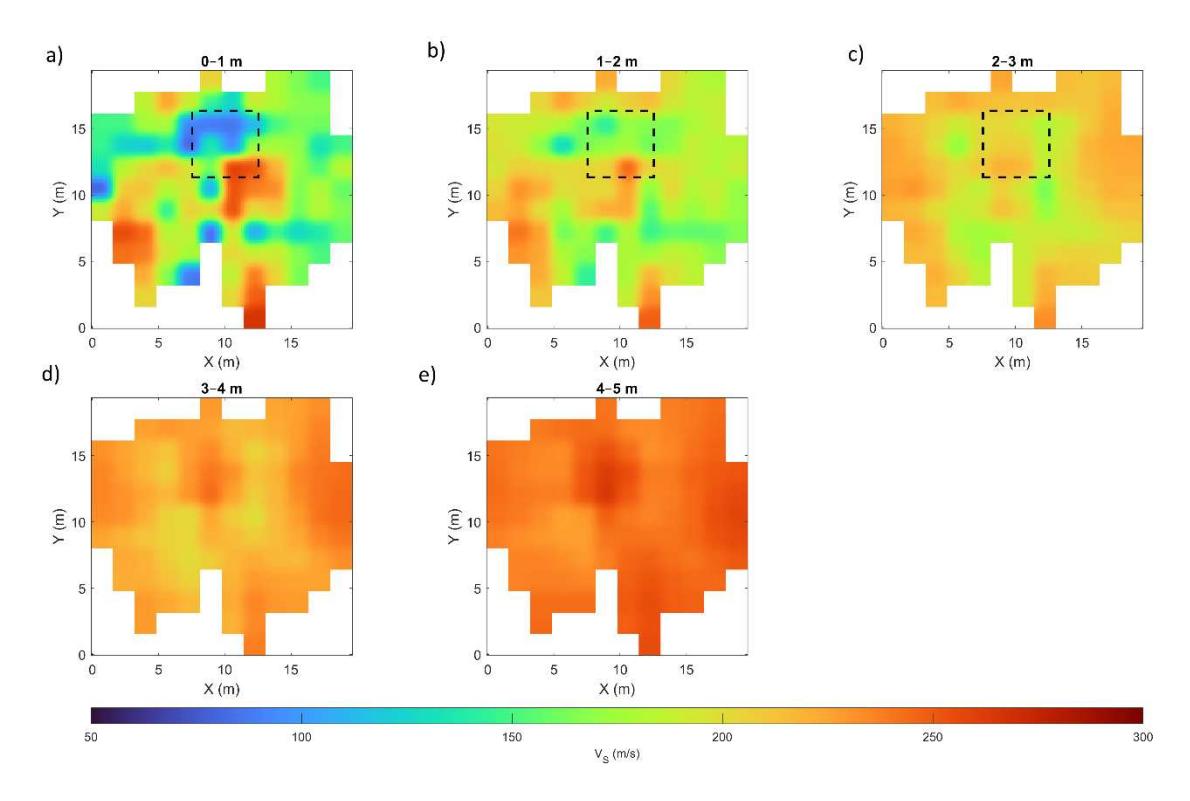


Figure 5-7 Shear-wave velocity maps for the constrained inversion model. (a–e) Vs distributions for depth intervals 0-1 m, 1-2 m, 2-3 m, 3-4 m, and 4-5 m.

In the constrained inversion (Figure 5-7) the velocity field appears smoother and more uniform over the area. At a depth of between 0 and 1 m, lower Vs values are observed, with a range of approximately 100 and 130 m/s, around the central part of the site, within the artificial sand body. Initially, the material is soft near the surface but becomes progressively stiffer towards depth. There also appears to be a small area of higher velocities located inside the square. The velocities reach 200-220 m/s starting from a distance of about 2 m, indicative of a change towards denser, more compact material. In general, the layers change smoothly, highlighting that the imposed constraints were able to keep the model geologically plausible.

#### 6. Conclusions

This thesis showed that seismic surface-wave interferometry can be used to characterize the near-surface from ambient noise recordings. Using a workflow with correlation, dispersion analysis, and inversion, a realistic shear-wave velocity (Vs) model was reconstructed for the artificial sand body at the CNR test site. The results show that the interferometric method can estimate the shallow subsurface without need for active sources.

The overall fits of both unconstrained and constrained inversions of the observed dispersion curves were similar, suggesting that the constraints level was not excessive. However, the stability and continuity of the two results were marked differently. The unconstrained inversion resulted in patches and sharp changes in velocities between neighboring cells, which is not easily interpretable in such a homogeneous context. On the other hand, the constrained inversion gave rise to a much smoother estimation, preserving the consistency of the sand body as well as the sorounding.

Within the 0–2 m depth range, the sand body is partially depicted. This is mainly due to interference of the urban traffic in the north of the site, creating directional noise that can bias interferometry method and erroneous estimated dispersion curves. It is important that the ambient noise field is uniform and arrives from distant sources in all directions in order to achieve cleaner and more symmetric interferometric results. The constrained inversion gave a more stable and realistic description of the substructure, while the broader pattern remained unchanged despite this localized effect. The estimated model (100–130 m/s at the surface and maybe 250–270 m/s at 4–5 m depth) is consistent with the prior knowledge of the site.

The results show that ambient-noise surface-wave analysis is valuable in shallow site investigations. Moreover, it is cheap, non-intrusive and has the potential for large scale near-surface characterization and monitoring.

#### References

- [1] K. Aki and P. G. Richards, *Quantitative Seismology*, 2nd ed. University Science Books, 2002.
- [2] G. D. Bensen, M. H. Ritzwoller, M. P. Barmin, A. L. Levshin, F. Lin, M. P. Moschetti, N. M. Shapiro, and Y. Yang, "Processing seismic ambient noise data to obtain reliable broad-band surface wave dispersion measurements," *Geophys. J. Int.*, vol. 169, no. 3, pp. 1239–1260, 2007.
- [3] D. Boiero, Surface Wave Tomography for Near-Surface Characterization. Ph.D. dissertation, Politecnico di Torino, 2009.
- [4] M. Campillo and A. Paul, "Long-range correlations in the diffuse seismic coda," *Science*, vol. 299, no. 5606, pp. 547–549, 2003.
- [5] M. Campillo and P. Roux, "Seismic imaging and monitoring with ambient noise correlations," in *Treatise on Geophysics*, 2nd ed., vol. 1, Elsevier, 2015, pp. 256–274.
- [6] S. Foti, C. G. Lai, G. J. Rix, and C. Strobbia, *Surface Wave Methods for Near-Surface Site Characterization*. CRC Press, 2014.
- [7] S. Foti, F. Hollender, F. Garofalo, D. Albarello, M. W. Asten, P.-Y. Bard, C. Comina, C. Cornou, B. R. Cox, G. Di Giulio, T. Forbriger, K. Hayashi, E. Lunedei, A. Martin, T. Matsushima, E. D. Mercerat, M. Ohrnberger, V. Poggi, and L. V. Socco, "Guidelines for the good practice of surface wave analysis: A product of the InterPACIFIC project," *Bull. Earthq. Eng.*, vol. 16, no. 6, pp. 2367–2420, 2018.
- [8] D. Halliday and A. Curtis, "Seismic interferometry, surface waves and source distribution," *Geophys. J. Int.*, vol. 175, no. 3, pp. 1067–1087, 2008.
- [9] B. O. Hardin and V. P. Drnevich, "Shear modulus and damping in soils: Measurement and parameter effects," *J. Soil Mech. Found. Div.*, vol. 98, no. SM6, pp. 603–624, 1972.
- [10] P. Lipinski, L. V. Socco, and S. Foti, "Shear wave velocity in situ measurements in sands using surface waves," *J. Appl. Geophys.*, vol. 145, pp. 120–132, 2017.
- [11] A. E. H. Love, Some Problems of Geodynamics. Cambridge Univ. Press, 1911.

- [12] Y. Luo, J. Xia, J. Liu, Y. Xu, Q. Liu, and C. Zeng, "Joint inversion of high-frequency surface waves and refraction first arrivals for near-surface shear-wave velocity profiles," *J. Appl. Geophys.*, vol. 121, pp. 1–11, 2015.
- [13] S. Nazarian and K. H. Stokoe, "In situ shear wave velocities from spectral analysis of surface waves," in *Proc. 8th World Conf. Earthquake Eng.*, vol. 3, pp. 31–38, 1984.
- [14] C. B. Park, R. D. Miller, and J. Xia, "Multichannel analysis of surface waves," *Geophysics*, vol. 64, no. 3, pp. 800–808, 1999.
- [15] L. Rayleigh, "On waves propagated along the plane surface of an elastic solid," *Proc. Lond. Math. Soc.*, vol. 17, no. 1, pp. 4–11, 1885.
- [16] N. M. Shapiro and M. Campillo, "Emergence of broadband Rayleigh waves from correlations of the ambient seismic noise," *Geophys. Res. Lett.*, vol. 31, no. 7, p. L07614, 2004.
- [17] R. Snieder, "Extracting the Green's function from the correlation of coda waves: A derivation based on stationary phase," *Phys. Rev. E.*, vol. 69, no. 4, p. 046610, 2004.
- [18] R. Snieder, "Extracting the Green's function of attenuating heterogeneous acoustic media from uncorrelated waves," *J. Acoust. Soc. Am.*, vol. 121, no. 5, pp. 2637–2643, 2007.
- [19] L. V. Socco, D. Boiero, S. Foti, and C. Strobbia, "Surface-wave analysis for building near-surface velocity models—Established approaches and new perspectives," *Geophysics*, vol. 75, no. 5, pp. 75A83–75A102, 2010.
- [20] K. Wapenaar, D. Draganov, R. Snieder, X. Campman, and A. Verdel, "Tutorial on seismic interferometry: Part 1—Basic principles and applications," *Geophysics*, vol. 75, no. 5, pp. 75A195–75A209, 2010.
- [21] M. Wilczynski, S. Foti, F. Garofalo, and P.-Y. Bard, "Combining active and passive surface wave methods for enhanced near-surface characterization," *J. Appl. Geophys.*, vol. 216, p. 105016, 2025.